Primary lung tumor segmentation from PET-CT volumes with spatial-topological constraint

Hui Cui, Xiuying Wang, Weiran Lin, Jianlong Zhou, Stefan Eberl, Dagan Feng, and Michael Fulham

Abstract

Purpose Accurate lung tumor segmentation is a prerequisite for effective radiation therapy and surgical planning. However, tumor delineation is challenging when the tumor boundaries are indistinct on PET or CT. To address this problem we developed a segmentation method to improve the delineation of primary lung tumors from PET-CT images.

Methods We formulated the segmentation problem as a label information propagation process in an iterative manner. Our model incorporates spatial-topological information from PET and local intensity changes from CT. The topological information of the regions was extracted based on the metabolic activity of different tissues. The spatial-topological information moderates the amount of label information that a pixel receives: the label information attenuates as the spatial distance increases and when crossing different topological regions. Thus the spatial-topological constraint assists accurate tumor delineation and separation. The label information propagation and transition model are solved under a random walk framework.

Results Our method achieved an average DSC of 0.848 ± 0.036 and HD (mm) of 8.652 ± 4.532 on 40 patients with lung cancer. The t-test showed a significant improvement (p-value < 0.05) in segmentation accuracy when compared to 8 other methods. Our method was better able to delineate

H. Cui X. Wang, W. Lin
Biomedical and Multimedia Information Technology (BMIT) research group, School of Information Technologies, University of Sydney, Sydney, Australia

J. Zhou
National ICT, Australia.

S. Eberl
Department of PET and Nuclear Medicine, Royal Prince Alfred Hospital, Sydney, Australia.

D. Feng
BMIT, School of Information Technologies, University of Sydney, Sydney, Australia. Med-X Research Institute, Shanghai Jiao Tong University, China.

M. Fulham
Department of PET and Nuclear Medicine, Royal Prince Alfred Hospital, Sydney, Australia. Sydney Medical School, University of Sydney, Australia

H. Cui
e-mail: hcui7511@uni.sydney.edu.au

tumors that had heterogeneous FDG uptake and which abutted adjacent structures that had similar densities.

Conclusions Our method, using a spatial-topological constraint, provided better lung tumor delineation, in particular, when the tumor involved or abutted the chest wall and the mediastinum.

Introduction

Positron emission tomography (PET) allows definition of a variety of tumors according to their metabolic profiles and characteristics, and so has been widely used in diagnosis, radiation therapy planning and treatment of diverse types of cancers [1]. For instance, ^{18}F-Fluorodeoxyglucose PET (FDG-PET) is commonly used in the evaluation of non-small cell lung cancer (NSCLC), for staging and to assess treatment response, because NSCLC has increased FDG uptake relative to surrounding normal lung. NSCLC is the most common type of lung cancer [2]. Accurate segmentation and delineation of lung tumors required for radiation therapy and surgical planning. For radiation therapy the aim is to deliver, with high-precision, the appropriate dose to the most metabolically active region of the tumor volume [3] while minimizing the radiation dose to surrounding tissue.

The manual delineation of tumor margins is operator dependent, time-consuming and relies on the expertise and experience of the operator. Whilst manual delineation of the tumor margin is the 'gold standard' a number of computer-assisted tumor segmentation methods have been investigated to automate the task and improve the efficiency of the process. A fixed threshold of the standard uptake value (SUV) which reflects FDG uptake [4], is widely used for automated tumor delineation from PET images. A 40% or 50% maximum SUV (SUV_{max}), or adaptive threshold based methods, are used to define the tumor margins [5]. However, there is no widely accepted SUV threshold for definition of the different tumor types [5]. Other PET segmentation methods, which have been used extensively include watershed and fuzzy c-means and they may fail to accurately delineate the tumor boundary because of the limited spatial resolution. Hatt and his team conducted systematic research on tumor delineation from PET and Fuzzy Locally Adaptive Bayesian (FLAB) [6, 7]. FLAB, however, requires a large number of seeds for reliable label estimation within a user pre-defined region of interest (ROI) (8). Further, the

capability for complex shape delineation in more difficult cases has to be further improved [8]. Foster et al suggested a novel method, using intensity affinity metric within the affinity propagation framework, to quantify and delineate the distributed lung inflammation in small animals [9].

The combination of PET and CT data improves segmentation algorithms [10]. An advantage of considering both modalities is that the co-segmentation results are more reliable [10]. Segmentation methods in PET-CT include our previous method under a Bayesian framework [11], an approach utilizing Markov random field (MRF) [12] and more recent methods using fuzzy connectedness frameworks [13]. Graph theory including graph cut (GC) [14] and the random walks algorithm (RW) [15] have also been the focus of extensive research in this area [16, 17] [8]. Among the graph based methods, the RW algorithm [15] is more attractive because it can capture the local affinity and solve the weak boundary problems found with various organs and imaging modalities [15, 18, 19]. Bagci et al. [8] proposed a co-segmentation method on the basis of RW and used the intensity information from PET and CT. Our approach, however, incorporates the abstract and compact representation of metabolic uptake regions in a PET image and it is a new area of research.

In this work, we extracted topological information of regions based on the metabolic activity of different tissues from PET. Then we incorporated the spatial and topological information in an iterative label information propagation process to adjust the probability map that was derived from the CT. Thus the spatial-topological constraint assists accurate tumor delineation and separation, in particular when the tumor is in close proximity to adjacent tissue with similar intensities.

Methods

Related work: Random Walk (RW)

In the RW [15], an input image $I = \{x_1, ..., x_i, ..., x_N\}$ is represented as an undirected graph G. In the graph $G = (\mathrm{V}, \mathrm{E})$, a node $v_i \in V$ corresponds to an image pixel x_i and an edge $e_{ij} \in E \subseteq V \times V$ connecting two neighboring nodes v_i and v_j is assigned a weight (as defined in Eq.1) to indicate the affinity of the two nodes.

$$w_{ij} = \exp(-\beta \|g_i - g_j\|^2) \qquad (1)$$

where g_i is the pixel intensity value at node v_i, and β is a weighting parameter. The greater the intensity differences, the lower the edge weight and the smaller ease with which the walker travels along the edge. The transition probability from node v_i to v_j is defined as

$$p_{ij} = w_{ij} \Big/ \sum_k w_{ik} \qquad (2)$$

Given predefined labels for the objects to be segmented, RW solves the segmentation by calculating the steady state probabilities that a random walker starting from a label and reaching the unlabeled nodes by iterating Eq.3 until convergence.

$$F(\mathrm{t}+1) = PF(\mathrm{t}) \qquad (3)$$

where $F(\mathrm{t})$ is the status at time t and $P = [p_{ij}]_{N \times N}$ is the transition matrix.

Proposed method

In RW, only the local neighboring intensity changes are considered during the transition process (by Eq.2). However, intensity information is not sufficient for an accurate segmentation, especially when the tumor boundary are indistinct or indiscernible on CT or when the tumor has heterogeneous FDG uptake on PET. Our hypothesis is that incorporating the spatial distance and topological relation of regions into the transition model will improve tumor delineation.

We use all the information from the PET-CT for lung tumor delineation. CT provides the important anatomical information and relatively high resolution intensities hence CT captures the local intensity changes. PET images, meanwhile, reflect tissue and tumor and so we extract the metabolically active regions to derive topological relations for the regions.

Iterative Label Information Propagation for Segmentation

We formulated the segmentation problem as a label information propagation process in an iterative manner. Given pre-defined labels $\{L_k \mid k = 1, ..., K\}$ for K objects to be segmented, the label information propagation from time t to $t+1$ is modeled as Eq.4

$$F(\mathrm{t}+1) = \gamma PF(\mathrm{t}) + (1 - \gamma) F(0) \qquad (4)$$

where the transition matrix P is calculated by Eq. (3) and (2) with CT intensities; the initial status $F(0)$ is a $N \times K$ matrix with $F_{ik}(0) = 1$ if x_i is initialized a label k and 0 otherwise; $F(t)$ is the status matrix where $F = [F_1, ..., F_i, ..., F_N]^T$ with $F_i = [F_{i1}, ..., F_{ik}..., F_{iK}]_{1 \times K}$ indicating the probability of a node x_i belonging to labels $\{L_k \mid k = 1, ..., K\}$; γ is a new spatial-topological factor defined from PET to describe the relation between node x_i and the labels. The detailed description and calculation of γ are discussed in the following section. Physically, the probabilities vector F_i can be seen as the amount of information that a node receives during the iteration, and γ adjusts the amount of information that the node receives in each step.

By iterating Eq.4 until global stable state is achieved, the final segmentation is achieved by solving Eq.5

$$F = (\mathrm{I} - \Lambda P)^{-1} \Lambda Y \qquad (5)$$

where $\Lambda = diag(\gamma)$. Based on the probability matrix F,

each of the unlabeled nodes is assigned a label with the largest probability.

Spatial-topological information

For the K objects to be segmented, we have K sets of labeled nodes $V_L = \bigcup_{k=1}^{K} V_{L_k}$. The spatial and topological factor γ between an unlabeled node and a set of labeled nodes V_{L_k} is defined with joint spatial distance term d and topological term δ as Eq.5:

$$\gamma(v_i, L_k) = d(v_i, V_{L_k})^{-1} \cdot \delta(v_i, L_k) \qquad (6)$$

Spatial distance term $d(v_i, V_{L_k})$ is the normalized shortest Euclidean distance between v_i and a labeled nodes set V_{L_k}, as defined as Eq.7:

$$d(v_i, V_{L_k}) = \min_{v_j \in V_{L_k}} \left\| v_i - v_j \right\| \qquad (7)$$

Topological term δ denotes the topological inclusion or exclusion relation of regions extracted from contour tree [20] [21] on PET image. The topological relations are extracted based on our previous work [22] that focused on the region of interest (ROI) to reduce the redundant information, by the following algorithm:

Algorithm: topological relations extraction

Input: ROI in PET image

Output: topological regions $\{r_x\}$ and topological relations of the regions

Step1: topological region extraction

    local extrema and saddle points detection;

    a topological region (Fig. 1(d)) is defined as a set of iso-contours (Fig. 1 (b)) between a local extreme and a saddle point (Fig. 1(c))

Step2: relation extraction

    exclusion: if two regions r_x, r_y split at a saddle point;

    inclusion: the region with local extrema is included in the region with saddle point
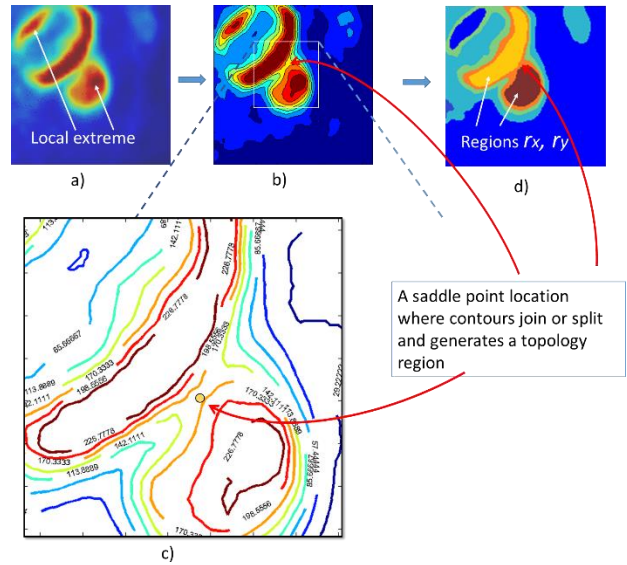

Fig. 1 The iso-contours and topology regions of a given PET image. (a) is a cropped PET image and local extreme; (b) is an illustration of the iso-contours; (c) is the enlarged region within the white box in (b) to see the iso-contours with iso-values. The orange iso-contours split from a saddle point. (d) the definition of topology regions.

With the topological relations, we assign values to the nodes in each topological region to reflect the relation with a topological region with labels. For a node v_i in r_x, the topological term $\delta(v_i, L_k)$ with respect to a region r_{L_k} with label L_k is defined as:

$$\delta(v_i \in r_x, L_k) = \begin{cases} \eta(r_x, r_{L_k}), & \text{inclusion} \\ \eta(r_x, r_y) \cdot \eta(r_y, r_{L_k}), & \text{exclusion} \\ 1, & \text{if } r_x = r_{L_k} \end{cases} \qquad (8)$$

where the value of η between two topology regions r_x, r_y is calculated as $\eta(r_x, r_y) = \min(\bar{g}_{r_x}, \bar{g}_{r_y}) / \max(\bar{g}_{r_x}, \bar{g}_{r_y})$ where $\bar{g}_{r_x}$ is the average SUV of region r_x.

The spatial and topological information represented by γ adjusts the amount of label information that a node receives during iterations as defined in Eq.4. If the two nodes belong to two topologically exclusive regions, the label information decreases when crossing these exclusive regions; thus it would assist accurate separation of the regions. In addition, the label information attenuates as spatial distance increases. The algorithm is summarized in Fig. 2.

1
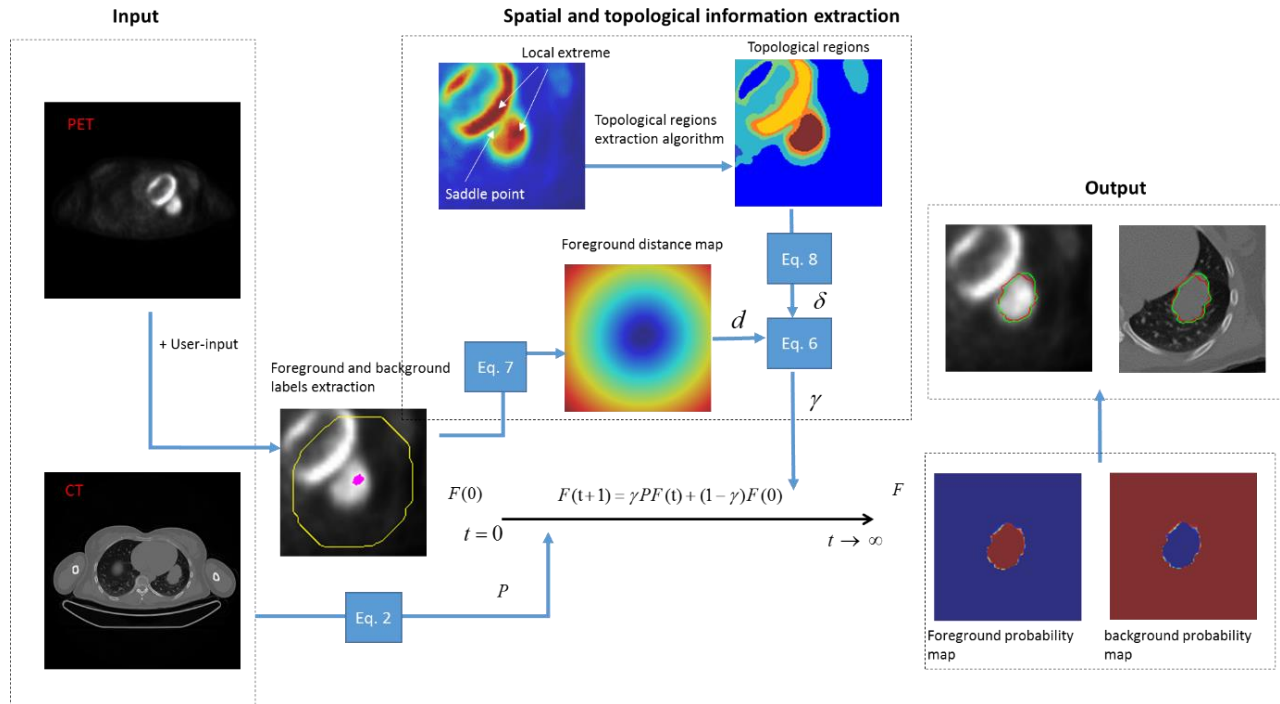
Fig. 2 Our proposed method is outlined graphically indicating the stepwise progression of the segmentation.

Patient studies

We used 40 PET-CT studies from patients with NSCLC. The scans were carried out on a Biograph TrueV 64 slice PET-CT scanner (Siemens Medical Solutions, Hoffman Estates, IL, USA). PET data were reconstructed into 168×168 matrices with pixel size of 4.07 mm $\times$ 4.07 mm. The CT data were reconstructed using a matrix of 512×512 pixels with pixel size of 0.98 mm $\times$ 0.98 mm. The slice thickness in PET-CT was 2 mm (20 studies) and 3 mm (20 studies). To obtain a spatial correspondence between the volumes in a common resolution space, PET volumes were registered to the corresponding CT volumes using the Insight Segmentation and Registration Toolkit (ITK) that is based on the affine transformation. Mutual information (MI) was used as the similarity metric and the average MI for the 40 patient studies was -0.595 $\pm$ 0.0517. Pre-processing and de-noising were not done and there was not a correction for partial volume effects.

In the 40 NSCLC studies, in 20 studies the tumors were located in the lung parenchyma, at a distance from adjacent structures such as the chest wall, mediastinum and pericardium. In the other 20 studies, the tumor boundaries were not easily 'discernible' that is where the tumor abutted and/or involved adjacent structures and/or had heterogeneous FDG uptake. In these latter 20 studies, in 16 the tumors abutted and / or involved the pleura and chest wall and in 4 the tumor was adjacent to or extended into the mediastinum. Manual delineation was performed by a senior clinical expert (who has read in excess of 15000 lung PET-CT studies), using PET and CT information, and the tumor boundaries were drawn on CT images. The manual delineation results was used as the "ground truth" (GT). The manual delineation results from another radiologist (referred as GT-2) were used for the inter-observer investigations.

Phantom studies

Twenty lung PET-CT phantom datasets were collected from the public RIDER collections [23] at the Cancer Imaging Archive. The target/background ratio was 4:1. The diameters of the 6 spheres were 10 mm, 13 mm, 17 mm, 22 mm, 28 mm and 37 mm. The PET data were reconstructed using a matrix of 128×128 with voxel size $2.73 \times 2.73 \times 3.27$ mm. The CT data were constructed using a matrix of 512×512 with voxels size $0.68 \times 0.68 \times 2.5$ mm.

Comparison methods

To evaluate the performance of approach we compared it to other methods for PET only, CT only and PET-CT co-segmentation algorithms. PET only methods included: 1) a threshold of 40% SUVmax on PET (referred to as RG40), 2) a threshold of 50% SUVmax (referred to as RG50), 3) an adaptive threshold method (referred to as RGa) [24], 4) Fuzzy c means (referred to as FCM) and (5) the tumor-customized downhill method (referred to as TCD) [25]. These methods were compared to validate the contribution of CT for tumor delineation. We also compared our method to CT only methods including RW [15] and RWR [26] to evaluate the contribution of spatial-topological information defined from PET. PET-CT co-segmentation methods included a tumor-background likelihood model [11] (referred as TBLM), the graph-based co-segmentation model using max flow optimization (referred as GC-co) [17], and the model under the RW framework (referred as RW-co)

[8].

Validation methods

To assess the accuracy of the proposed method, we calculated the spatial overlap and shape dissimilarity between the segmentation results and GT by Dice's Similarity Coefficient (DSC) and Hausdorff Distance (HD). DSC was defined as

$$DSC(U_1, U_2) = \frac{2|U_1 \cap U_2|}{|U_1| + |U_2|} \qquad (9)$$

where U_1 is the segmented volume, and U_2 is the GT volume. The DSC value is 1 for a perfect segmentation.

HD was defined as

$$HD(U_1, U_2) = \max\{\sup_{i \in S_1} \inf_{j \in S_2} d(i, j), \sup_{j \in S_2} \inf_{i \in S_1} d(i, j)\} \qquad (10)$$

where S_1 and S_2 denote the boundary of the segmented volume and the GT volume, and $\sup$ represents the least subset element and $\inf$ the greatest subset element; d is the Euclidean distance between point i and j. A low HD value indicates high segmentation accuracy.

Implementation, initialization and parameter settings

Our algorithm was implemented with MATLAB R2013a on a PC with 3.50GHz Intel(R) Core(TM) i7-4770K CPU and 16.0GB memory, running a 64-bit Windows operating system. The method was implemented on 2D slices. The Graph Analysis Toolbox [27] was used to build the weighted image graph and solve the linear equations for RW, RW-co and our method. The fixed and adaptive thresholding methods and FCM were implemented using the functions in ITK. RWR were based on the public code found on the authors' personal websites [28]. TCD and TBLM were our previous work. GC co-segmentation was implemented using the max flow library [14].

We set K=2 to indicate the tumor/foreground and background. A user-input seed was manually provided to indicate the targeted tumor for segmentation. And the foreground and background seeds were obtained as: firstly the local maximum SUV ($SUV_{\max}^{local}$) was obtained automatically by comparing the user indication with its neighbouring voxels. The RG40. RG50, RGa, FCM and TCD methods were implemented starting from the $SUV_{\max}^{local}$. For our method and the graph-based methods, RWR and RW, the pixel set with foreground labels was obtained by performing region growing from $SUV_{\max}^{local}$ and stopped at 95% $SUV_{\max}^{local}$. And the pixels with background labels were defined as the contour of a background region. The background region was obtained by continuing region growing from the detected foreground labels and stopped at

40% $SUV_{\max}^{local}$ and further enlarged with a band whose width is equal to the radius of the foreground region.

For the comparison methods under RW framework - RW, RWR, RW-co and our method - the parameter β in the weighting function (6) was set to be 60, the same as RW [15], RWR [29] and RW-co [17]. The parameters for GC-co were according to the values in the original paper [8].

Results

Sensitivity studies

To evaluate the initialization sensitivity, we compared the segmentation results when the foreground and background criterion was set as: (0.95, 0.4), (0.9, 0.4), (0.95, 0.3) and (0.9, 0.3). The results with respect to DSC are shown in Fig. 3 and identifies that our method was not sensitive to the seeds criterion.
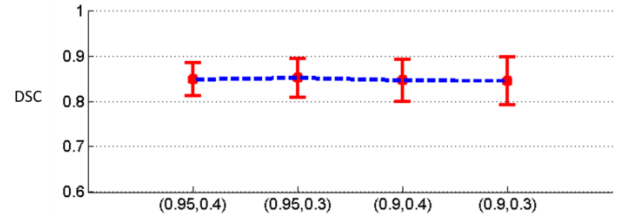
**Fig. 3**. Seeds sensitivity investigation in regard to the average DSC over the 40 patient studies

Evaluation of clinical cases

The segmentation results of one patient study with a small parenchymal tumor are shown in Fig. 4. The tumor volume (measured according to GT) was about 2.73 ml. The contrast between tumor and surrounding tissues was relatively low on PET. FCM failed to segment the tumor and resulted in leakage, and the other three methods on PET, RG40, RG50 and TCD resulted in smaller delineations. Our method achieved a DSC of 0.843 and the second best was RW with the DSC of 0.841.

The segmentation results of two cases where the tumors involved the chest wall are shown in Figures 5 and 6. In the first case our method achieved the best result with a DSC of 0.918 while the second best was TBLM with the DSC of 0.887; for the second case our method achieved the best DSC of 0.823 while second best was TBLM with a DSC of 0.811. RG50 resulted in smaller tumor definition and the RW and RWR on CT resulted in leakage into the chest wall.

The tumor in Fig. 7 was much larger with a volume of about 264.28 ml and it had heterogeneous FDG uptake. SUV based methods excluded the parts of the tumor that had low SUVs (areas of necrosis or cystic change) and failed to delineate the whole tumor. TBLM and our method achieved better results with the DSCs of 0.879 and 0.892 respectively.
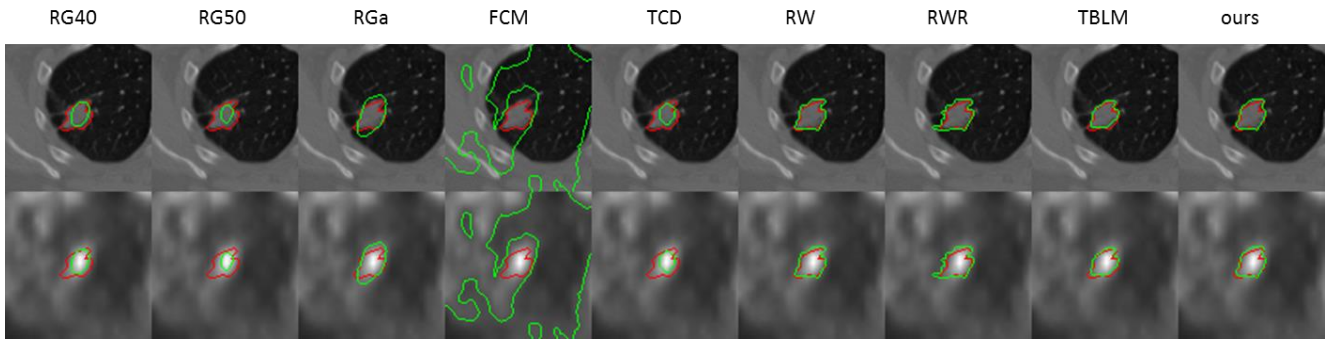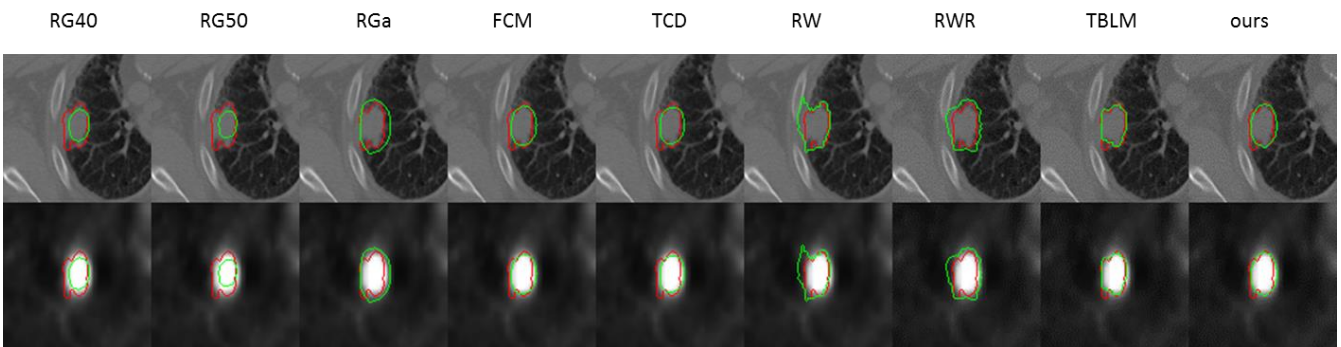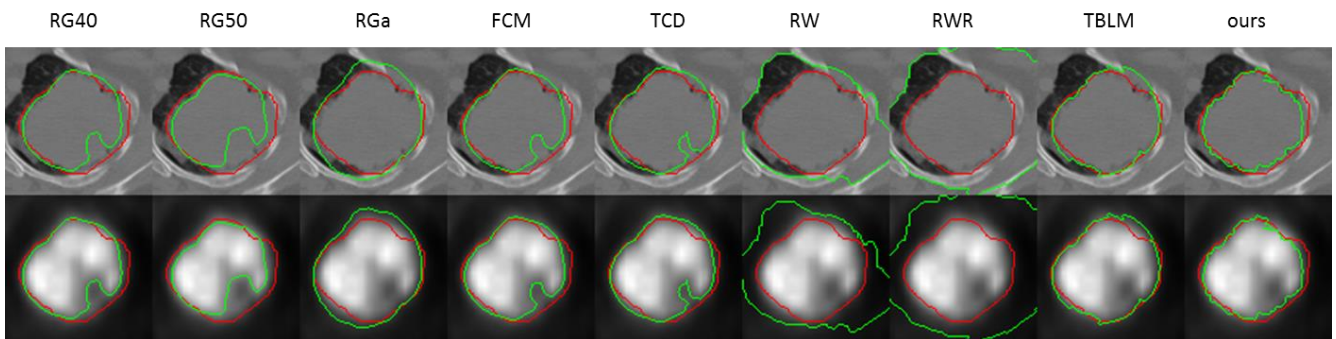
Fig. 4 Cropped tumor delineation results of a study with small tumor on CT (first row) and PET (second row) in the transaxial plane; segmentation results are shown in green and GT in red.
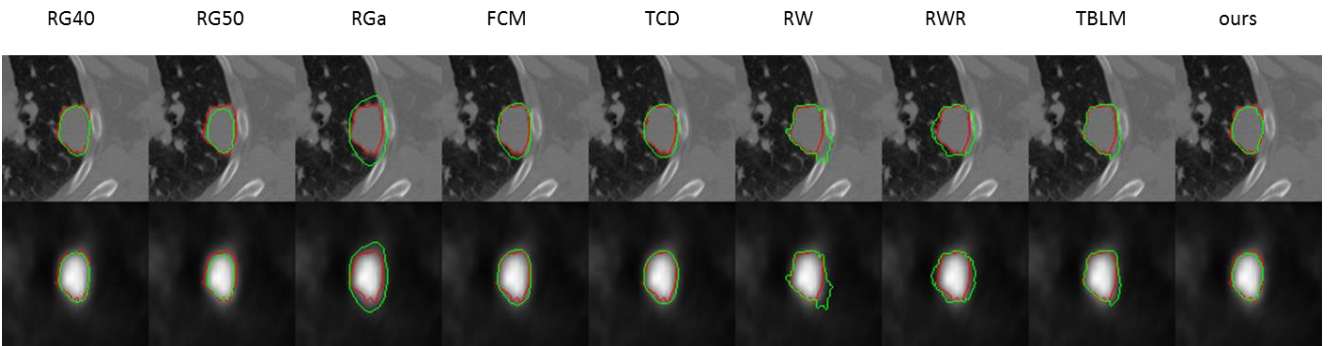
Fig. 5 Cropped tumor delineation results of one case with the tumor involving the chest wall on CT (first row) and PET (second row) in transaxial plane; segmentation results are shown in green and GT in red.
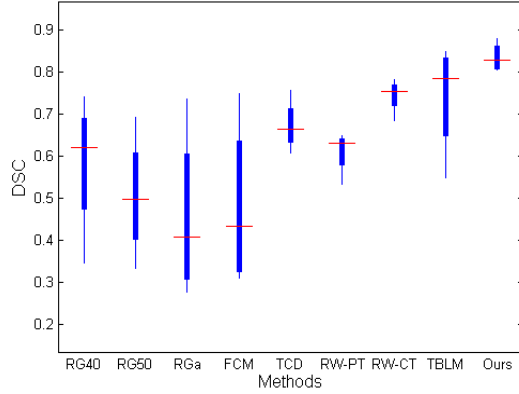

Fig. 6 Cropped tumor delineation results of one case with the tumor involving the chest wall on CT (first row) and PET (second row) in transaxial plane; segmentation results are shown in green and GT in red.


Fig. 7 Cropped tumor delineation results for one case where the tumor boundaries on CT are difficult to discern and the tumor has non-uniform (heterogeneous) FDG uptakes; segmentation results are shown in green and GT in red.

Among the 40 studies there were 16 cases where the tumor abutted or involved the pleura / chest wall and 4 had tumor adjacent to or extending into the mediastinum. The results of spatial overlap measurement (DSC) of these chest wall and mediastinum studies are shown statistically with box-plots in Figures 8 and 9. These plots show that our method achieved consistently better segmentation for all the studies that had indistinct or indiscernable boundaries.

Fig. 8 Spatial overlap comparison by DSC of 4 cases which had tumors adjacent to or extending into the mediastinum
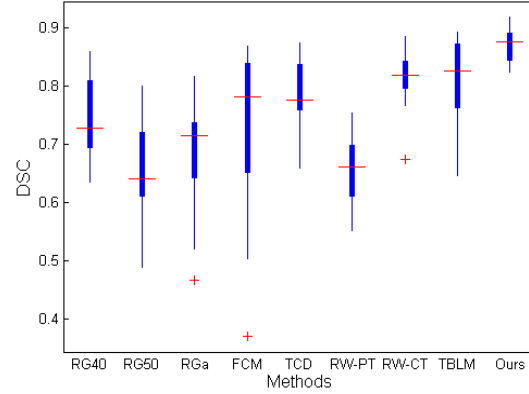
Fig. 9 Spatial overlap comparison by DSC of 16 cases with the tumors abutting the pleura/chest wall

Overall, our method had the best results over the 40 studies based on the DSC and HD (see Table 1). TBLM and RW were ranked the second and the third. The methods based on solely PET achieved lower accuracy than the other CT and PET-CT based methods. We performed Students paired t-Test with a two-tailed distribution and our method had a significant statistical improvement (p-value < 0.05) when compared to the other methods (see Table 2).

**Table 1** Mean DSC and HD over all 40 cases with respect to GT

Methods	DSC (mean ± SD)	HD (mm) (mean ± SD)
RG40	0.671 ± 0.120	16.562 ± 15.093
RG50	0.603 ± 0.098	15.131 ± 12.140
RGa	0.574 ± 0.193	22.139 ± 21.647
FCM	0.608 ± 0.209	28.083 ± 24.778
TCD	0.723 ± 0.086	11.692 ± 7.943
RW	0.806 ± 0.082	12.601 ± 5.009
RWR	0.781 ± 0.078	18.451 ± 8.865
TBLM	0.813 ± 0.069	10.220 ±7.586
Our Method	**0.848 ± 0.036**	**8.652 ± 4.532**

**Table 2** T-Test (alpha =0.05) of eight methods with proposed method over the 40 cases with respect to GT

Methods	p-values (DSC)	p-values (HD)
RG40	3.729E-09	1.500×10^{-3}
RG50	7.413E-15	6.580×10^{-4}
RGa	7.310E-09	4.390×10^{-4}
FCM	3.161E-07	4.771E-05
TCD	1.881E-10	1.032×10^{-3}
RW	3.380×10^{-4}	8.372E-07
RWR	8.869E-10	5.232E-07
TBLM	1.847×10^{-3}	2.6528×10^{-2}

To illustrate the contribution of the defined spatial-topological factor in our method when compared to RW, segmentation results and the foreground and background probability maps of one study is shown in Fig. 10. For this case, the tumor boundary was readily discernible on CT. RW failed in the accurate tumor boundary delineation and our method achieved more concentrated foreground and background probability maps. This is also seen from the probability maps of RW, RWR and our method as shown in Fig. 11.

The running time of the algorithm was 1.99 seconds and the average running time for the 40 studies from the beginning to end was 28.618 seconds.
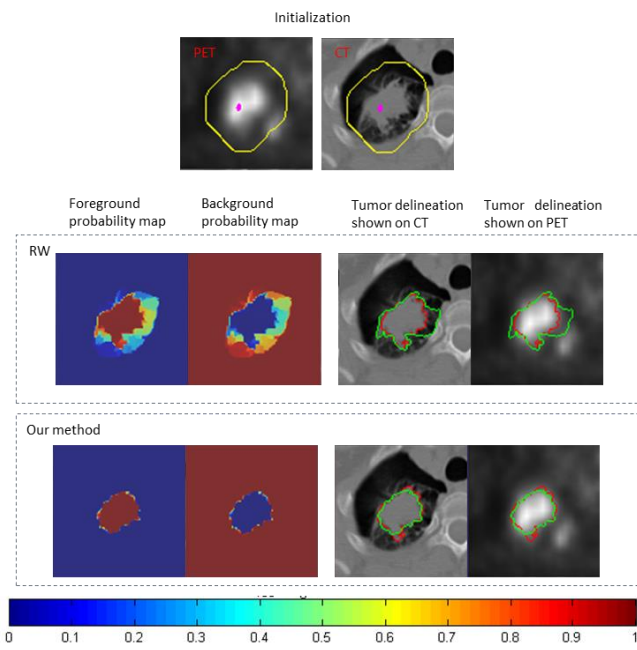
Fig. 10 One study evaluated by RW and the proposed method, with the iniltilization, the foreground/background maps and the delieation results.
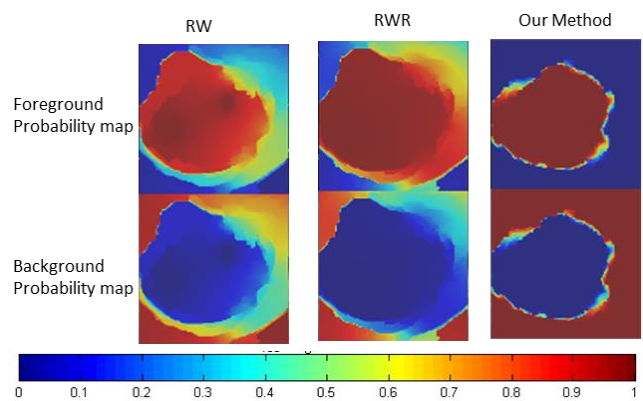
Fig. 11 Zoomed foreground and background probability maps of the RW-based methods for the study in Fig. 7

Inter-observer agreement and validation

To further evaluate the proposed method, the manual delineation results GT-2 were also used for validation. The inter-observer agreement between GT-2 and GT was measured by DSC, and the average DSC was 0.85 ± 0.059 over 40 datasets. The segmentation results by DSC with respect to GT and GT-2 were illustrated in Fig. 12.
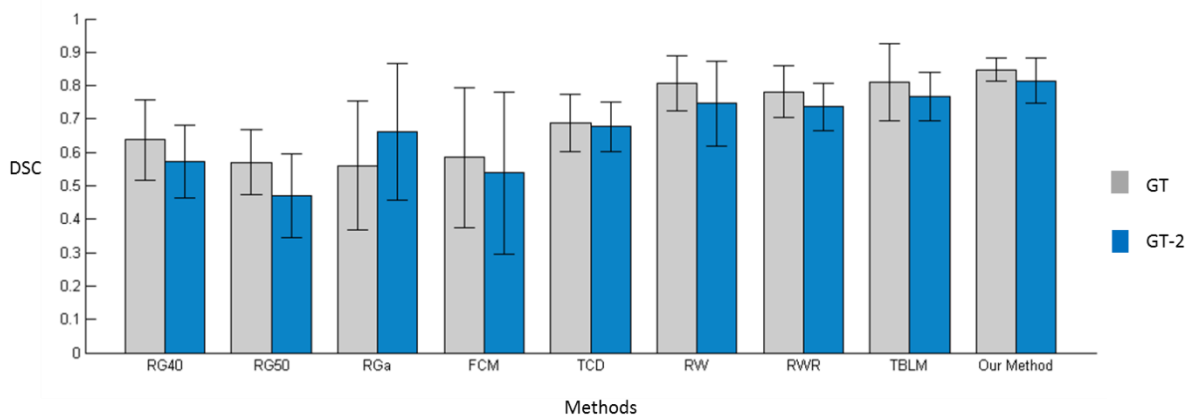

Fig. 12 Inter-observer validation over the 40 clinical studies.

Comparison with other graph based co-segmentation methods

We also compared our method to two other graph-based co-segmentation methods, RW-co and GC-co that were segmented by GT and GT-2. As shown in Fig. 13, our method consistently achieved higher accuracy in terms of DSC and HD. And the t-test between our method and RW-co demonstrated that the improvement was statistically significant (p=0.0289).
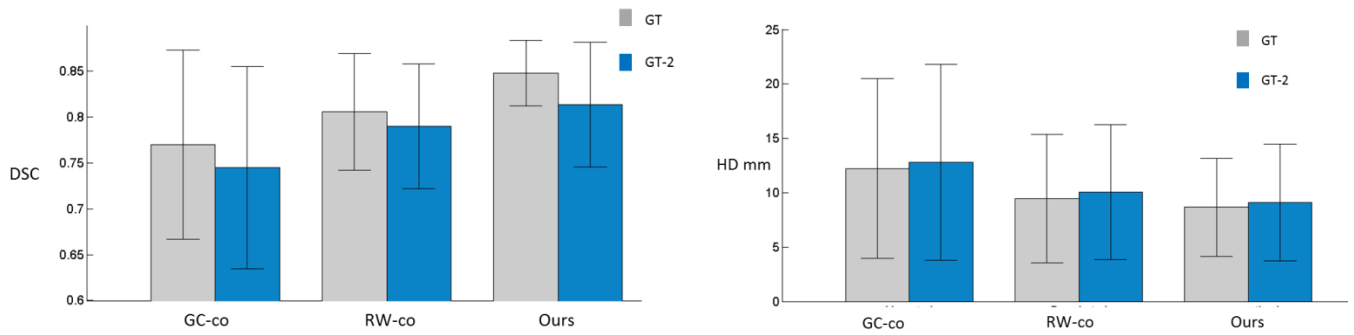
Fig. 13 DSC and HD comparison with two other graph based co-segmentation emthods with respect to the GT and GT-2.

Phantom evaluation

For the 20 phantom datasets, each with 6 simulated tumors of different sizes, our method achieved DSC (mean ± SD) of 0.850 ± 0.072 and outperformed the second best method RW-co that had 0.825 ± 0.078. As shown in Fig. 14, RW-co failed to delineate the entire tumor.
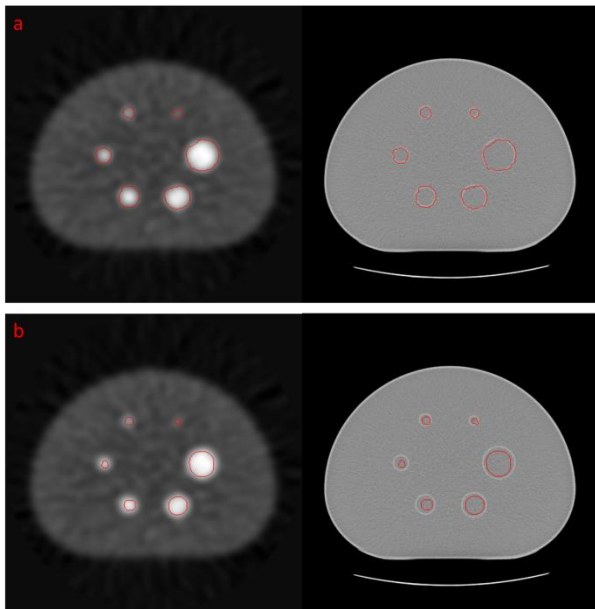
Fig. 14 The phantom results shown on PET and CT. (a) is our results and (b) is the result of RW-co.

Discussion

Our main finding is that our proposed label information propagation model, with the incorporation of intensity information from CT and spatial-topological information from PET, can delineate the entire tumor when the tumor was in close proximity to adjacent tissue with similar intensities.

The main contribution of the proposed method is the incorporation of the spatial-topology constraint (STC). The

STC played critical role when the tumor involved / abutted the chest wall or was adjacent to or involving mediastinum. In such instances, solely depending on CT intensity leads to leakage to the tissue surrounding the tumor. Our spatial-topological information moderated the amount of label information that a pixel receives: the label information attenuates as the spatial distance increases and when crossing different topological regions. And thus, the spatial-topological information helped to appropriately define the tumor boundary. For instance in Fig. 7, the tumor abutted to the chest wall and both shared similar intensities. As shown in Fig. 11, probability map of RW partially included the chest wall. In contrast, in our method the STC attenuated the label information when crossing different metabolic regions and thus our method produced a more concentrated map than RW and RWR (see Fig. 11).

The sharp local CT intensity changes at the discernable boundary were the major factor for delineating the tumor boundary. Compared with the tumor boundary delineations by PET only methods, our method was able to better maintain the tumor shape reflected on CT. For instance the case in Fig. 4 where the tumor was located in the lung parenchyma, the CT intensity contributed to the shape delineation.

When using both PET and CT information, the co-segmentation methods may produce a smoothed segmentation result. Our spatial-topological factor attenuated the CT definition and may have smoothed the segmentation (see Fig. 10). As suggested by Bagci et al. [8], this "smoothness" was due to the anatomical and functional regions not always having identical lesion contours for instance, the disparity between the anatomical lesion size and the extent of FDG uptake. Segmentation accuracy might be reduced in our method if the topological information is not properly extracted from PET, for example, when PET images have low signal-to-noise ratios and the tumor-background contrast also decreases if the tumor is smaller than 20 to 30 mm [30] [31]. In such studies, the topology from current methods would contain many small "noisy" regions and therefore may lead to incorrect definition of regional relations [32].

In the future work, we would like to validate the proposed model on other tumor types and we plan to extend the model to segment multiple objects such as the left and right ventricular cavity, myocardium and papillary muscles on

cardiac images.

Conclusions

We propose a new label information propagation model for tumor segmentation, which correlates CT intensity and the spatial-topological from PET. We evaluated our method on 40 NSCLC patient studies. The results show that the incorporation of the spatial-topological information with the intensity then contributed to better tumor delineation, especially where the tumor is involves the chest wall or mediastinum and when the boundaries between tumor and adjacent tissues are indistinct.

Conflict of interest

Hui Cui, Xiuying Wang, Weiran Lin, Jianlong Zhou, Stefan Eberl, Dagan Feng, and Michael Fulham declare that they have no conflict of interest.

References

1. MacManus, M., et al., *Use of PET and PET/CT for Radiation Therapy Planning: IAEA expert report 2006–2007.* Radiotherapy and Oncology, 2009. **91**(1): p. 85-94.
2. Ahmedin Jemal, F.B., Melissa M. Center, Jacques Ferlay, Elizabeth Ward and David Forman, *Global cancer satatistics.* CA: A Cancer Journal for Clinicians, 2011. **61**(2): p. 69-90.
3. Kirov, A. and L. Fanchon, *Pathology-validated PET image data sets and their role in PET segmentation.* Clinical and Translational Imaging, 2014. **2**(3): p. 253-267.
4. Simona, B.-H. and E. Peter, *18F-FDG PET and PET/CT in the Evaluation of Cancer Treatment Response.* The Journal of Nuclear Medicine, 2009. **50**(1): p. 88-99.
5. Boellaard, R., *Mutatis Mutandis: Harmonize the Standard!* Journal of Nuclear Medicine, 2012. **53**(1): p. 1-3.
6. Hatt, M., et al., *A Fuzzy Locally Adaptive Bayesian Segmentation Approach for Volume Determination in PET.* IEEE Transactions on medical imaging, 2009. **28**(6): p. 881-893.
7. Hatt, M., et al., *Accurate Automatic Delineation of Heterogeneous Functional Volumes in Positron Emission Temography for Oncology Applications.* International Journal of Radiation Oncology Biology Physics, 2010. **77**(1): p. 301-308.
8. Bagci, U., et al., *Joint segmentation of anatomical and functional images: Applications in quantification of lesions from PET, PET-CT, MRI-PET, and MRI-PET-CT images.* Medical Image Analysis, 2013. **17**(8): p. 929-945.
9. Foster, B., et al., *Segmentation of PET Images for Computer-Aided Functional Quantification of Tuberculosis in Small Animal Models.* Biomedical Engineering, IEEE Transactions on, 2014. **61**(3): p. 711-724.
10. Foster, B., et al., *A review on segmentation of positron emission tomography images.* Computers in Biology and Medicine, 2014. **50**(0): p. 76-96.
11. Wang, X., et al., *Lung Tumor Delineation Based on Novel Tumor-Background Likelihood Models in PET-CT Images.* Nuclear Science, IEEE Transactions on, 2014. **61**(1): p. 218-224.
12. Han, D., et al., *Globally Optimal Tumor Segmentation in PET-CT Images: A Graph-Based Co-Segmentation Method*, in *Inf Process Med Imaging*. 2011. p. 245-256.
13. Xu, Z., et al. *Fuzzy Connectedness Image Co-Segmentation for Hybrid PET/MRI and PET/CT Scans*. in *Computational Methods for Molecular Imaging Workshop, Medical Image Computing and Computer-Assisted Intervention (MICCAI)* 2014. Boston.
14. Boykov, Y., O. Veksler, and R. Zabih, *Fast Approximate Energy Minimization via Graph Cuts.* IEEE Trans. Pattern Anal. Mach. Intell., 2001. **23**(11): p. 1222-1239.
15. Grady, L., *Random walks for image segmentation.* IEEE Transactions on Pattern Analysis and Machine Intelligence, 2006. **28**(11): p. 1768-1783.
16. Qi, S., et al., *Optimal Co-Segmentation of Tumor in PET-CT Images With Context Information.* Medical Imaging, IEEE Transactions on, 2013. **32**(9): p. 1685-1697.
17. Han, D., et al., *Globally Optimal Tumor Segmentation in PET-CT Images: A Graph-Based Co-Segmentation Method.* Information processing in medical imaging : proceedings of the ... conference, 2011. **22**: p. 245-256.
18. Grady, L., et al., *Random walks for interactive organ segmentation in two and three dimensions: Implementation and validation*, in *Medical Image Computing and Computer-Assisted Intervention*. 2005. p. 773-780.
19. Chen, M., et al., *Random Walk-based Automated Segmentation For The Prognosis of Malignant Pleural Mesothelioma*, in *IEEE International Symposium on Biomedical Imaging: From Nano to Macro*. 2011. p. 1978-1981.
20. Carr, H., J. Snoeyink, and U. Axen, *Computing contour trees in all dimensions.* Comput. Geom. Theory Appl., 2003. **24**(2): p. 75-94.
21. Zhou, J., *Gaining Insights Into Volumetric Data Visualization: A Semi-Automatic Transfer Function Generation Approach Using Contour Tree Analyses*. 2012, Germany: LAP LAMBERT Academic Publishing.
22. Cui, H., et al., *Topology constraint graph-based model for non-small-cell lung tumor segmentation from PET volumes*, in *IEEE International Symposium on Biomedical Imaging (ISBI)*. 2014. p. 1243-1246.
23. *RIDER Phantom PET-CT: UNIVERSITY OF WASHINGTON*. Available from: https://wiki.cancerimagingarchive.net/display/Public/RIDER+Collectio ns.
24. Black, Q.C., et al., *Defining a radiotherapy target with positron emission tomography.* International Journal of Radiation Oncology Biology Physics, 2004. **60**(4): p. 1272-1282.
25. Ballangan, C., et al., *Automated Delineation of Lung Tumors in PET Images Based on Monotonicity and a Tumor-Customized Criterion.* IEEE Transactions on Information Technology in Biomedicine, 2011. **15**(5): p. 691-702.
26. Kim, T.H., K.M. Lee, and S.U. Lee, *Nonparametric higher-order learning for interactive segmentation*, in *IEEE Conference on Computer Vision and Pattern Recognition*. 2010. p. 3201-3208.
27. Grady, L., *The Graph Analysis Toolbox: Image processing on arbitrary graphs*. 2003: Boston University, Boston, MA, Tech. Rep. TR-03-021.
28. Kim, T.H. *Generative Image Segmentation using Random Walks with Restart*. Available from: http://cv.snu.ac.kr/thkim/RWR_ECCV08/index.html.
29. Kim, T.H., K.M. Lee, and S.U. Lee, *Generative Image Segmentation Using Random Walks with Restart*, in *European Conference on Computer Vision*. 2008. p. 264-275.
30. Kinahan PE, D.R., Wanner-Roybal M, Bidaut LM, Armato SG, Meyer CR, McLennan G., *PET/CT Assessment of Response to Therapy: Tumor Change Measurement, Truth Data, and Error.* Translational Oncology, 2009. **2**(4): p. 223-230.
31. Shah, B., et al., *Intra-reader reliability of FDG PET volumetric tumor parameters: effects of primary tumor size and segmentation methods.* Annals of Nuclear Medicine, 2012. **26**(9): p. 707-714.
32. Zhou, J., C. Xiao, and M. Takatsuka, *A multi-dimensional importance metric for contour tree simplification.* Journal of Visualization, 2013. **16**(4): p. 341-349.